Study of cleavage fracture in ferritic stainless steels Part II: Cleavage micro-mechanisms and critical stresses

Lucie Jacquet, Rafael Estevez, Muriel Braccini, Maximilien Libert, Nicolas Meyer, Marc Mantel

Study of cleavage fracture in ferritic stainless steels
Part II: Cleavage micro-mechanisms and critical stresses.

Lucie JACQUET[a,b], Rafael ESTEVEZ[a], Muriel BRACCINI[a*], Maximilien LIBERT[b], Nicolas MEYER[b], Marc MANTEL[a,b]

[a] Univ. Grenoble Alpes, CNRS, Grenoble INP, SIMaP, 38000 Grenoble, France
[b] Research center, Ugitech, 73400 Ugine, France
* corresponding author: muriel.braccini@simap.grenoble-inp.fr

Abstract:
Cleavage fracture and the mechanisms involved in different ferritic steel model microstructures are investigated according to grain sizes, precipitates and solute atoms in the matrix. For each case, one of these parameters is varied. Estimation of the critical stress for cleavage was investigated and discussed: it is shown to be determined from a simple Griffith inspired analysis or by employing the Smith's description. The description to adopt depends on careful analysis of the involved mechanisms. This aims at better understanding the governing parameters of the Ductile to Brittle Transition Temperature (DBTT) and to suggest routes for alloys processing to reduce the DBTT in ferritic steels.

Keywords: ferritic stainless steels; cleavage; critical stress; ductile to brittle transition temperature

1. Introduction

Ductile to Brittle Transition (DBT) is a problem of concern, particularly in ferritic steels where this transition can happen at ambient temperature or for higher temperature. Thus, a lot of studies have been devoted to this topic, by investigating the influence of various parameters such as the alloy composition or the grain size: on a macroscopic point of view, increasing the carbon and/or nitrogen content tends to increase the Ductile to Brittle Transition Temperature (DBTT) [1-3], while decreasing the grain size decreases the DBTT [3-5]. However, at a microscopic scale, these trends are more cumbersome because a given composition will lead to different microstructures in terms of precipitation, grain size and ferrite solid solution composition depending on the thermomechanical treatment of the alloy. For instance, the influence of carbon and nitrogen concentration on the DBTT is not the same if those atoms are as interstitial atoms in the ferrite solid solution, decreasing its ductility, or as coarse carbide or nitride precipitates [1,3]. Ferritic stainless steels are often stabilized to get carbon and nitrogen atoms in order to avoid chromium carbides or nitrides precipitation and the associate chromium depletion. Niobium and titanium are the most used stabilizing elements and then their influence on the DBTT in ferritic stainless steels has also been studied [1,3,6,7]. On one hand, Ti leads to smaller grain size which tends to decrease the DBTT, but it also precipitates in liquid steel as TiN large particles with angular shape which seems to be detrimental for the fracture behavior [7]. On the other hand, Nb precipitates as small and round carbo-nitrides, but those particles tend to limit recrystallization and fine grain formation during thermomechanical treatments [1,3]. Then, the choice between Nb or Ti as stabilizing element regarding the DBTT is not straightforward, and will depend on thermomechanical treatments.

In order to better understand the influence of those parameters on the DBTT and rupture by cleavage, micromechanics models have been proposed considering one of the different steps in

cleavage failure: (i) crack initiation, (ii) crack propagation along cleavage plans inside the grain and (iii) finally propagation inside adjacent grains [8,9]. Pioneer models were based on dislocation mechanisms. The Zener-Stroh's model considers stress concentration due to edge dislocations pile-up on a grain boundary as a possible mechanism for cleavage crack initiation in BCC metals [10-12]. The Cottrell's model assumes a microcrack initiated at the intersection of two slip planes and calculates the condition for its propagation [13]. Both models lead to an expression with a dependence to the grain size of the local critical stress. Nevertheless, other microstructure parameters can influence the cleavage rupture, and, after observations of cracked grain boundary carbides in mild steel, Smith proposed a modification of the Cottrell model [14-15]. Considering a crack in a grain boundary carbide, an energy balance analysis is carried out to derived the energy release rate for crack nucleation. Smith then established a criterion for crack initiation within the grain, by accounting for the prescribed stress and its intensification in the vicinity of the grain boundary by a dislocation pile-up. He obtained an expression for the critical stress where grain size as well as grain boundary carbide thickness intervene. Finally, crack cleavage can initiate by failure or decohesion of brittle particles inside the grains [16-17], which is often observed in ferritic steels [9]. In this case the different steps of the cleavage failure can be interpreted as microstructure barriers to overcome [9,17]: the propagation of the crack inside the grain implies the crossing of the particle/matrix interface while the propagation to the adjacent grains requires the crossing of grain boundaries. In this multiple barriers model, critical stress calculation for each step is based on a Griffith's approach where the toughness of the barrier, particle/matrix interface or grain boundary, is considered as well as the particle size or the grain size respectively.

Critical stress for cleavage is estimated from the loading magnitude at the onset of final breakdown. This short review on micromechanics models show that it will depend on microstructure parameters: not only grain size but also precipitation properties such as particles location, size and shape. The purpose of the present work is to investigate the effect of those microstructure parameters on the cleavage mechanism in ferritic stainless steels. In the accompanying Part I [18], model microstructures are described along with the thermomechanical treatments that have been developed in order to attempt to modify and control microstructure parameters such as precipitation or grain size. Here, the mechanical characterizations of those model microstructures are presented with the aim to analyze cleavage micro-mechanisms, quantify critical stress for cleavage and link this critical stress to DBTT.

2. Methods:

a. Model microstructures

Six model microstructures were elaborated based on the composition of AISI 444 ferritic stainless steel. All the alloys under consideration contains 18 % Cr, 2 % Mo, and 0.015 % of both carbon and nitrogen. In order to investigate the effect of precipitation on cleavage fracture, three of the microstructures were stabilized, with Nb or Ti, and different thermal treatments were conducted. Those treatments and the characterizations of the obtained microstructures are detailed in the companion paper of this study [18]. Here only the microstructure parameters of interest for the cleavage fracture mechanisms are described and reported in table 1.

The unstabilized microstructures were obtained from the same composition but through different thermal treatments. For the Cr microstructure the last recrystallization treatment at 1000 °C followed by quenching lead to a grain size of 80 µm. We also observed presence of coarse carbide and nitride particles inside the grains and fine intergranular precipitates remain. With a recrystallization treatment at higher temperature (1050 °C), the Cr0 microstructure shows a larger

grain size of 250 µm but fine precipitates are only detectable at the grain boundaries. Finally, for the CrP microstructure, a treatment at 850 °C after a recristallization at 1000 °C lead to larger precipitates inside the grains and at the grain boundaries, while the grain size is similar to the one in the Cr microstructure.

Both Ti and Nb-stabilized microstructures were elaborated. The purpose to add stabilizing elements is to get interstitial atoms, carbon and nitrogen, forming Ti or Nb carbo-nitrides instead of chromium ones and so avoiding Cr-depletion zones. Thus, after the recrystallization treatment at 1000 °C, TiN precipitates and Nb(C,N) precipitates are present respectively in the Ti microstructure and in the Nb one. The two microstructures have similar grain size (between 60 and 80 µm) but the precipitates are larger in the Ti microstructure: TiN particles are up to 4.2 µm large, while Nb(C,N) are smaller than 1.7 µm. A second Nb-stabilized microstructure was elaborated thanks to a recrystallization at 1250 °C followed by a very slow cooling, down to 1000 °C and a 30 min maintain before quenching. The obtained microstructure, NbG, has a larger grain size of 600 µm with precipitates slightly larger than in the Nb microstructure: up to 2.4 µm.

Microstructure	**Grain size (µm)**	**Precipitation**		
		Nature	**Location**	**Max. size**
Cr0	250	M_2X	Grain boundaries	30 nm
Cr	80	M_2X $M_{23}C_6$	Grain boundaries Inside the grains	30 nm 2.5 µm
CrP	70	M_2X $M_{23}C_6$	Grain boundaries Inside the grains	1 to 6 µm long 3.5 µm
Ti	80	TiN	Inside the grains	4.2 µm
Nb	60	Nb(C,N)	Inside the grains	1.7 µm
NbG	600	Nb(C,N)	Inside the grains	2.4 µm

Table 1. Model microstructures parameters. Max. size corresponds to the particles maximum size in Cr0, Cr et CrP microstructures and to the lower bound of the 2% coarsest particles in Ti, Nb and NbG microstructures.

b. Mechanical characterizations

Charpy impact tests were performed on 10 x10 x 55 mm^3 V-notched specimen in order to determine the Ductile to Brittle Transition Temperature (DBTT) for each microstructure. The loading direction was parallel to the rolling and cold working longitudinal direction. Samples were maintained 15 minutes at the test temperature before performing the test, in a furnace for high temperature tests and in a cooling bath in ethanol for tests at temperature below ambient conditions. 12 to 20 tests were performed for each microstructure at temperature ranging between -70 °C and 450 °C. The absorbed energy experimental data were then fitted by the following empirical equation [19], to highlight the main DBTT characteristics:

$$KV(T) = A + \frac{B-A}{2}\left(1 + \tanh\left(\frac{T - T_{DBT}}{D}\right)\right), \quad (1)$$

where A and B are the absorbed energy values at the lower and the upper shelf respectively; D the steepness of the transition and T the temperature. T_{DBT} corresponds to the DBTT.

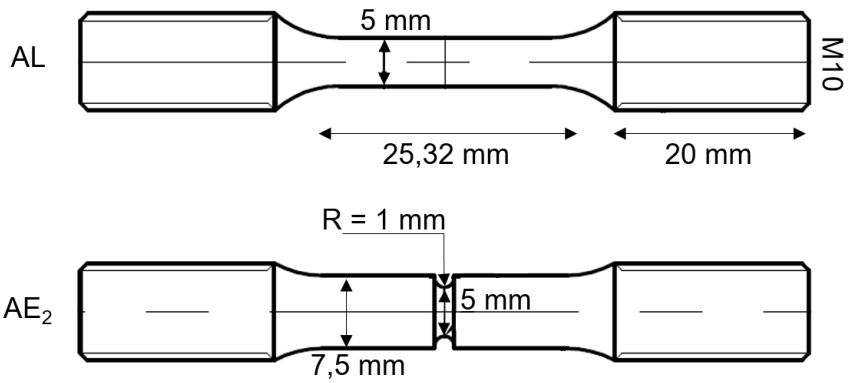

Figure 1. Specimen for mechanical characterizations: specimen (on the left) and AE specimen (on the right) for quasi-static tensile tests.

Quasi-static tensile tests were also performed on axisymmetric specimen, with and without notches as presented in figure 1. Samples were machined so that the tensile direction corresponds to the rolling and cold-working longitudinal direction. Un-notched ("smooth") specimens (AL) were used to identify mechanical behavior while notched specimens (AE) were used to determine the critical stress at which cleavage fracture takes place in each microstructure. Indeed, in the notched section of the AE specimen, the stress triaxiality is larger than in a smooth specimen, and cleavage rupture is favored [20]. Tensile tests were performed on a Roell and Kortaus machine with a 200 kN load cell and at 1 mm/min displacement rate. Tests were conducted at 20 °C and at -40 °C thanks to an environmental chamber adapted onto the testing machine. On both AL and AE samples, axial displacement was measured thanks to a digital images correlation method. For AE sample, the radial displacement at the notch region was also recorded and then post-processed with an image treatment automatized with Python scripts (see figure 2). In this program, sample edges in the notch area are detected (figures 2(b) and 2(c)), after a correction on the sample verticality (figure 2(d)) diameters along this area are calculated and the minimum value is selected (figure 2(e)).

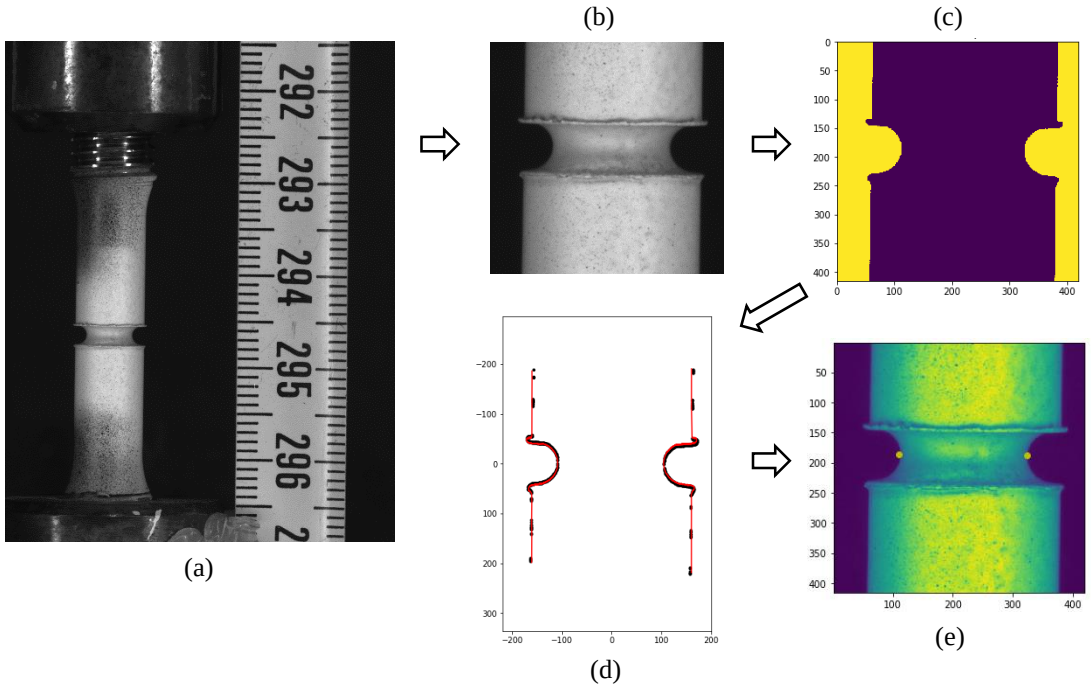

Figure 2. Image analysis for radial displacement measurement on AE specimen. (a) AE specimen image; (b) Cropped image; (c) Threshold; (d) Edge detection; (e) Minimum diameter location.

Fracture surfaces were observed at different magnifications using binocular device, optical microscope and scanning electron microscope, in order to characterize the fracture mechanism, ductile or brittle, or mixed. Moreover, on brittle fracture surfaces, cleavage fracture initiation site can be identified thanks to a method described by Henry and Plateau [21]. This method consists in following the cleavage "rivers" that converge to the initiation site. In order to determine the critical stress for cleavage, a method was used based on the calculation of the maximum principal stress σ_I at this initiation location, at the onset of cleavage failure [22]. For this, a numerical model based on finite elements method has been prepared in Abaqus [23]. Because of the symmetry of the problem, only a quarter of the AE specimen needs to be modeled (see figure 3(a)). Eight-nodes axisymmetric elements with reduced integration (CAX8R) were used with a refined size down to 40 µm in the notch area. For each test, the elastic-plastic constitutive law corresponding to the microstructure is implemented and the maximum principal stress σ_I distribution along the minimum section is extracted (see figure 3(b)). Thanks to the fracture surface analysis, the location of the cleavage fracture initiation site can be reported in terms of radius in this section and the corresponding stress is then considered as the critical stress for cleavage σ_c (see figures 3(c) and 3(d)).

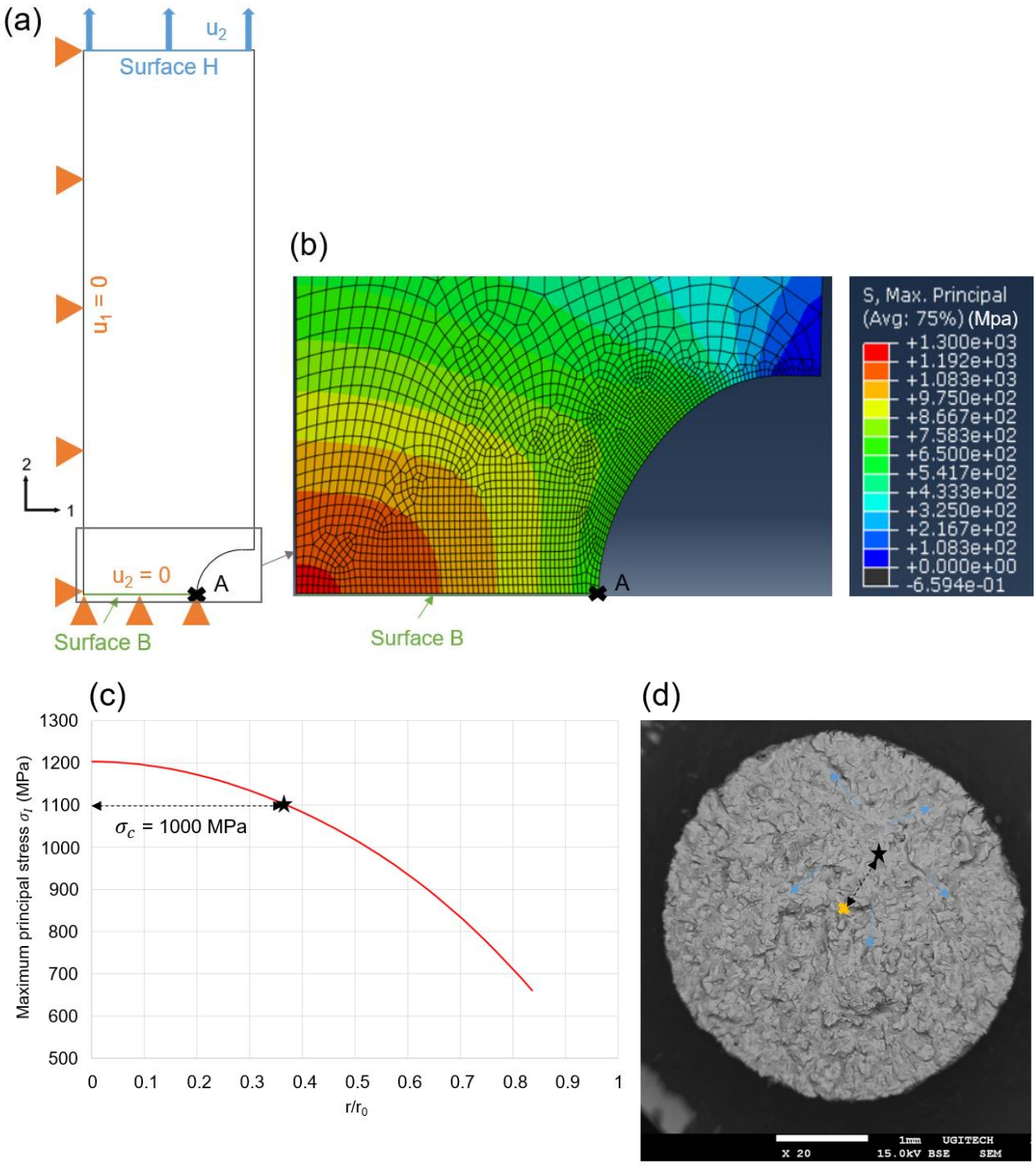

Figure 3. Method to determine the critical stress for cleavage rupture σ_c. (a) Numerical model of AE specimen; (b) σ_I maximum principal stress profile in the notch area; (c) σ_I maximum principal stress plotted along the minimum diameter section; (d) fracture surface image of Ti-H2-1 sample where the cleavage fracture initiation site (black star) and the center of the fracture surface (yellow cross) are identified. Blue arrows indicate the crack propagation directions from the initiation site.

3. *Results*

a. Variation of the DBTT for the six model microstructures

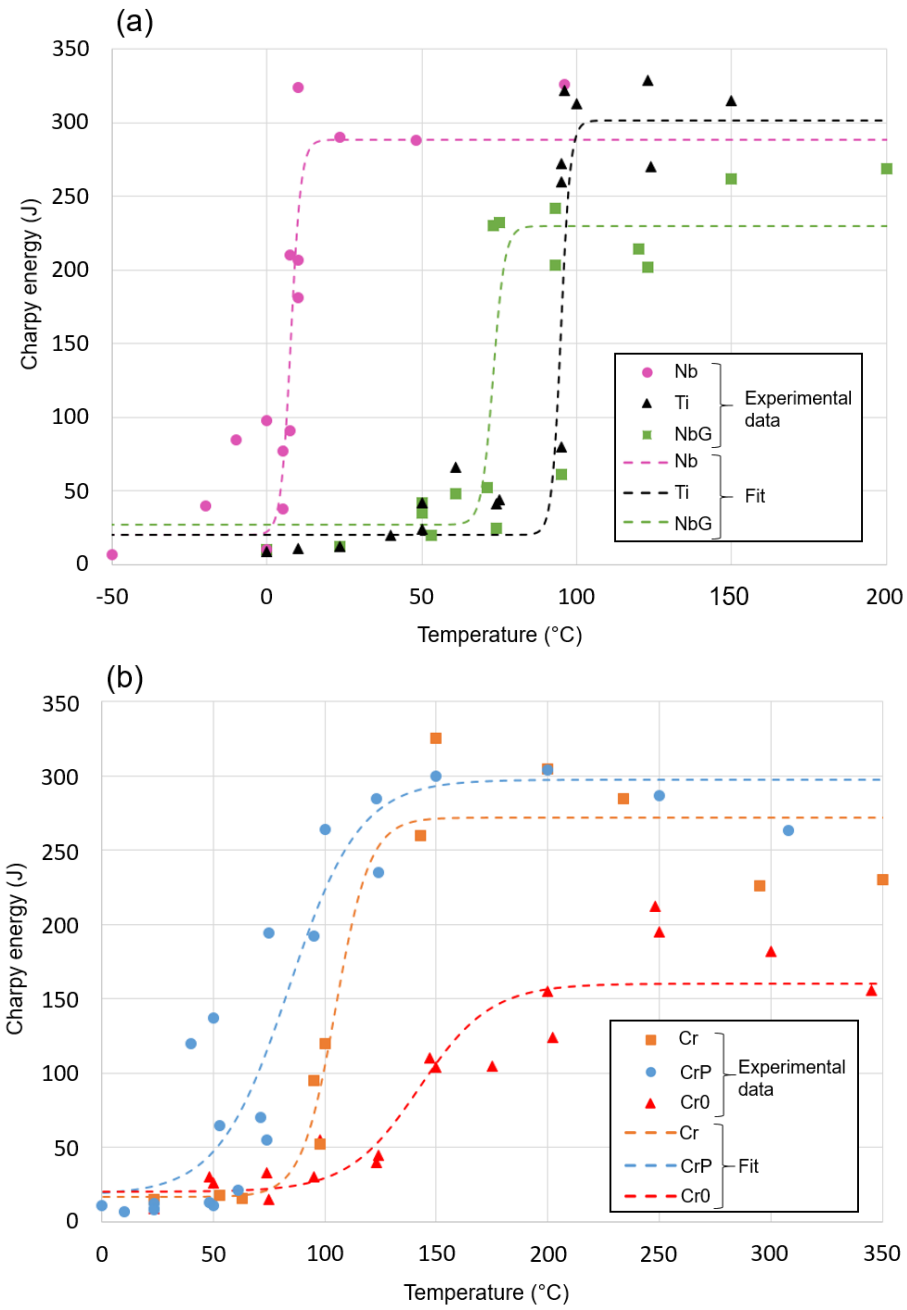

Figure 4. Ductile to Brittle Transition curves in absorbed energy: a. stabilized microstructures; b. unstabilized microstructures.

The Charpy impact tests conducted between -70 °C and 450 °C lead to the Ductile to Brittle Transition curves presented in figure 4. In figure 4(a), the variation of the Charpy fracture energy for the stabilized microstructures are reported. The Nb microstructure exhibits the lower transition temperature, at 8 °C, while NbG and Ti have a transition temperature at 75 °C and 95 °C respectively (see table 2). For the unstabilized microstructures (figure 4(b)), CrP has the lower DBTT, equal to 82 °C, close to the values of Ti and NbG, while the two other microstructures exhibit larger transition temperatures: 105 °C for Cr and 142 °C for Cr0. Cr0 has the highest transition temperature, moreover its absorbed energy on the ductile plateau is quite smaller than the ones for the other microstructures (about half the other values).

Stabilized microstructures		**Unstabilized microstructures**	
Microstructure	DBTT	Microstructure	DBTT
Ti	95 °C	Cr	105 °C
Nb	8 °C	CrP	82 °C
NbG	75 °C	Cr0	142 °C

Table 2. Ductile to Brittle Transition Temperature (DBTT) for the different microstructures.

b. Tensile properties

Quasi-static tensile tests were conducted on AL smooth axisymmetric specimen with a displacement rate of 1 mm/min, which corresponds to a strain rate of around 7×10^{-4} s^{-1}. From those mechanical characterizations performed at 20 °C and -40 °C various properties can be collected: the yield strength $R_{p0.2}$ and the tensile strength R_m, the elongation before fracture A%. Conventional stress-strain curves obtained at 20 °C are presented in figure 5 and mechanical properties for the model microstructures are reported in table 3.

A small stress peak can be observed on some of the microstructures according to the temperature and the high and low values of those peaks are reported in table 3 as R_{phigh} and R_{plow} respectively. In mild steel, this behavior is often observed and refers to a Lüders effect or static strain ageing: it corresponds to a strain localization due to the pinning of dislocations on solute atoms. In particular, carbon and nitrogen interstitial atoms are often identified as responsible for this phenomenon that tends to increase when the temperature decreases [24-25] as we can observe on the data collected in table 3. The NbG microstructure does not exhibit this peak stress at the tested temperatures. This can be explained by its larger grain size. Indeed, the Lüders peak stress decreases when the grain size increases until disappearing for large grain size [26].

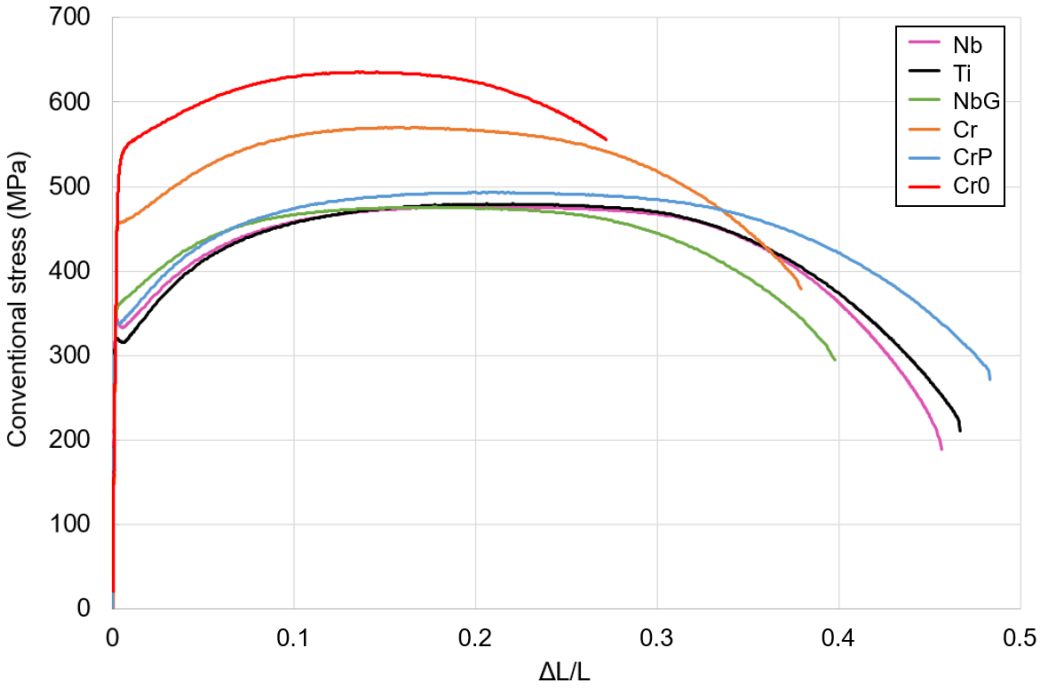

Figure 5. Conventional stress-strain curves of the six microstructures at room temperature.

Microst	Temperature	Peak stress?	$R_{p0,2}$ (MPa)	R_{pLow} (MPa)	R_{pHigh} (MPa)	R_m (MPa)	A(%)
Ti	20 °C	Yes	321 ± 2	317 ± 1	320 ± 2	481 ± 3	49 ± 2
	-40 °C	Yes	372 ± 8	372 ± 8	380 ± 15	540 ± 6	43 ± 1
Nb	20 °C	Yes	338	333	341	476	47
	-40 °C	For one test	414 ± 8	409	416	568 ± 12	43 ± 2
NbG	20 °C	No	356 ± 6	/	/	474 ± 3	39 ± 2
	-40 °C	No	403 ± 3	/	/	520 ± 8	13 ± 3
CrP	20 °C	Yes	338 ± 1	335 ± 2	346 ± 12	493 ± 2	47 ± 2
	-40 °C	Yes	388 ± 1	388 ± 1	395 ± 3	550 ± 2	45 ± 3
Cr	20 °C	Yes	450 ± 10	450 ± 10	455 ± 11	562 ± 11	38 ± 1
	-40 °C	Yes	524 ± 1	523 ± 1	530 ± 2	632 ± 2	31 ± 5
Cr0	20 °C	No	539 ± 5	/	/	633 ± 4	26 ± 3
	-40 °C	Yes	522 ± 13	516 ± 20	559 ± 50	707 ± 3	23 ± 2

Table 3. Mechanical properties of the model microstructures at 20 °C and at -40 °C.

From table 3 we notice that the stabilized microstructures and the CrP one have similar properties in terms of yield strength and tensile strength. They all exhibit a ductile fracture at both temperatures and their elongations before facture are equal or larger than 40 %, except for NbG at -40 °C. For this microstructure at -40 °C, the elongation before fracture is 13 % and the fracture surface is mixed with a large ductile area in the center but a thin brittle fracture surface at the edge. The Cr and Cr0 microstructures have a larger yield strength and tensile strength than the other microstructures. For Cr0, which has the largest yield strength at room temperature, this can be explained by solute hardening due to the presence of carbon and nitrogen atoms in the supersaturated ferrite solid solution [18]. For Cr, residual carbon and nitrogen atoms are present in the supersaturated solid solution, but in smaller fraction than in Cr0 [18] which is in agreement with a lower yield strength than in Cr0. Finally, Cr0 has the lowest elongations before fracture and

exhibits brittle fracture at both temperatures, while Cr shows brittle fracture at -40°C but ductile fracture at 20 °C. Those results and observations can be correlated to the Charpy impact tests. Indeed, the Cr0 microstructure, that has the highest DBTT, exhibits a brittle fracture during the tensile tests at 20 °C, while all the other microstructures fail in a ductile mode.

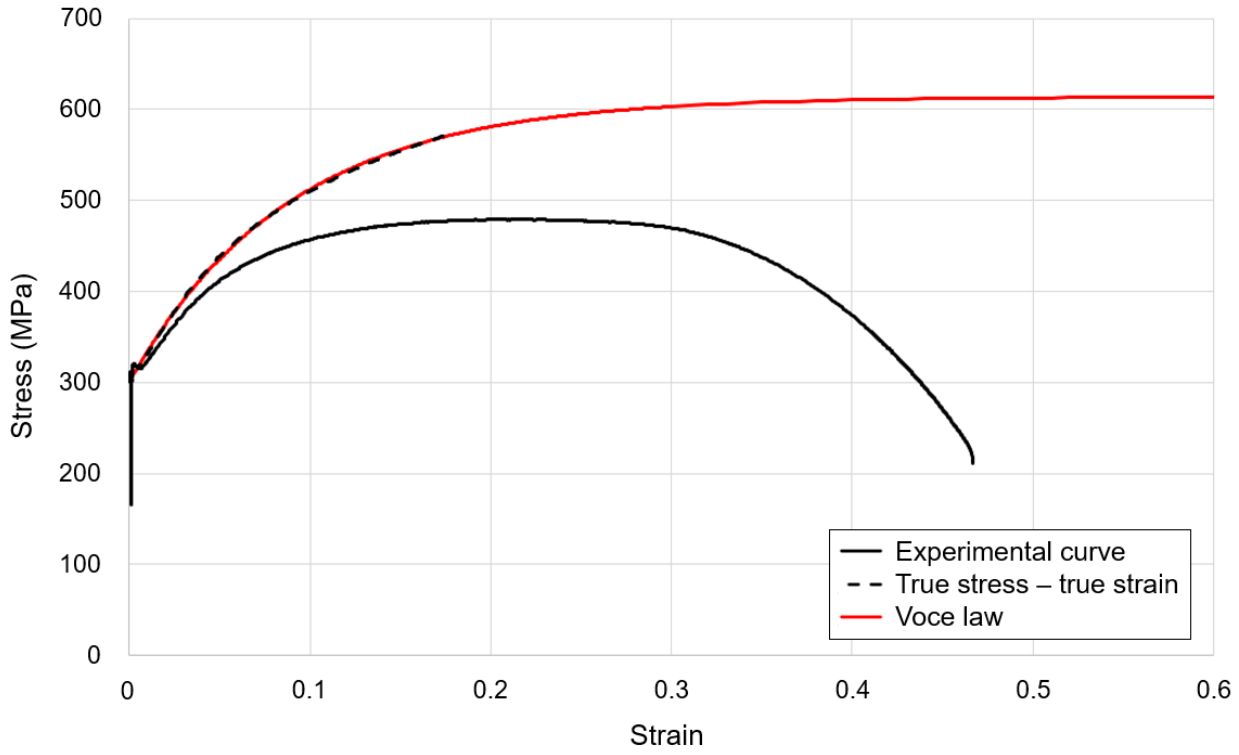

Figure 6. True stress-true strain curve for Ti microstructure at 20 °C: experimental data and Voce law (Q =313 and b =11.37).

Loading curves obtained on the smooth tensile specimen were also used to identify the hardening response of the alloys. True stress and true strain were calculated as follows:

$$\varepsilon_r = \ln\left(1+\frac{\Delta L}{L_0}\right) \quad \text{and} \tag{2.1}$$

$$\sigma_r = \frac{F}{S_0}\left(1+\frac{\Delta L}{L_o}\right) \quad , \tag{2.2}$$

where F and ΔL are respectively the load and the axial displacement, L_o and S_o the initial gage length and the initial section of the specimen. Those equations are valid only if the deformation is uniform in the sample and for isochoric plasticity, then only the part of the curve before necking was considered. Moreover, a correction was applied to the peak stress that is not part of the plastic behavior of the material [27] (see figure 6). A simple Voce-type isotropic hardening law was chosen

$$R(p) = R_0 + Q\left[1-\exp(-bp)\right] \quad , \tag{3}$$

where p is the cumulated plastic strain, $R(p)$ the related isotropic hardening and R_o the yield strength. The Voce's parameters Q and b are identified for each microstructure to capture the plastic response (table 4). Such a fit is exemplified in figure 6 for the Ti microstructure.

Microstructure	R_o (MPa)	Q (MPa)	b (MPa)
Ti	300	313	11.37
Nb	319	288	11.1
NbG	346	249	11.78
CrP	321	303	11.6
Cr	441	285	9.19
Cr0	533	282	8.86

Table 4. Voce parameters Q and b to fit the tensile tests for each microstructure at 20 °C.

c. Fracture behavior and critical stress for cleavage

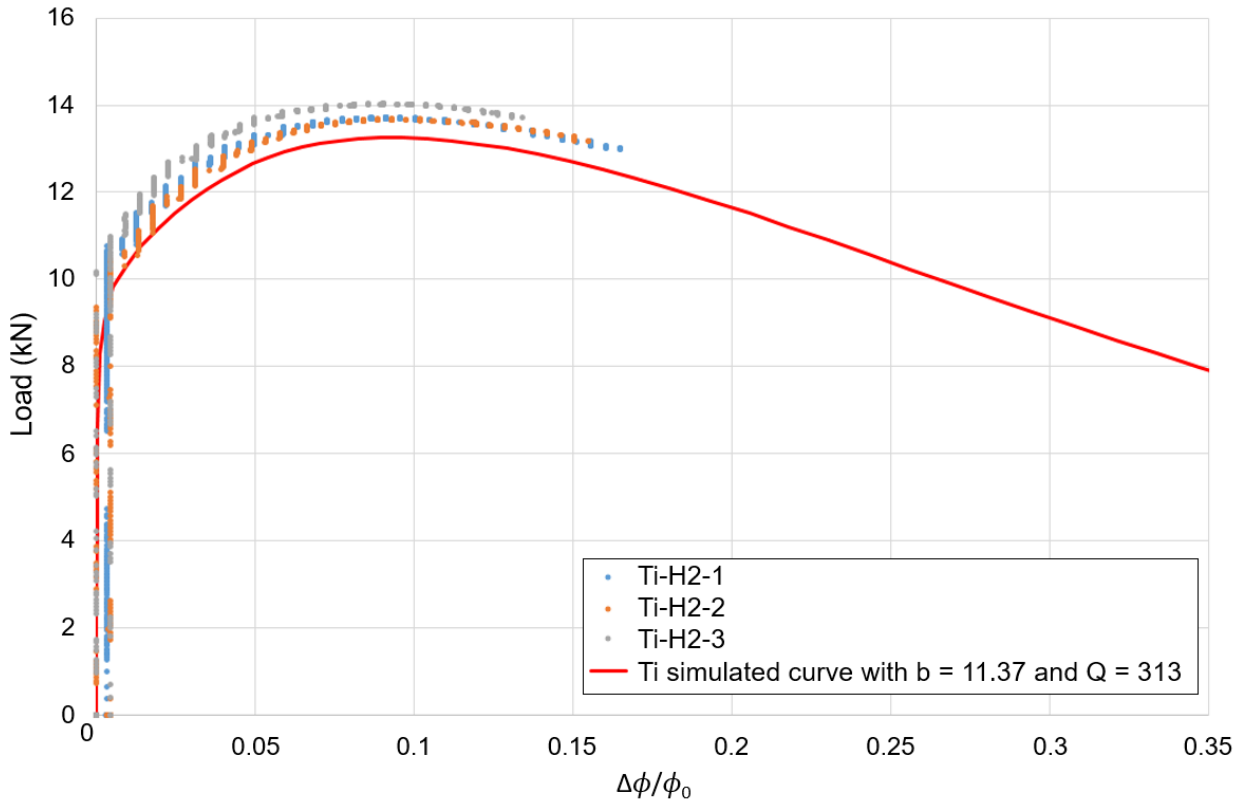

Figure 7. Load vs diameter reduction curves for Ti AE_2 specimen and the predicted curve of the tensile test using the Voce parameters given in Table 4.

In order to study the cleavage behavior of the model microstructures, tensile tests were conducted on notched axisymmetric specimen (AE) at both 20 C° and -40 °C. For each condition, 3 to 5 tests were performed. Fracture surfaces analysis revealed cleavage fracture for each

microstructure at both temperatures, except for the Nb microstructure at 20 °C (see figure 7), which is consistent with the fact that this microstructure has a DBTT quite lower than the other ones.

Before extracting the critical stress for cleavage, predicted load-diameter reduction curves were compared to experimental ones. The predicted curves were obtained using the numerical model for AE specimen described in section 2 with an elastic modulus E of 200 GPa and a Poisson's ratio ν of 0.3, a Von Mises yield criterion and the Voce isotropic hardening law identified on the corresponding smooth specimen. Nevertheless, the predicted curves did not fully capture the experimental data satisfactorily (see figure 7 for Ti microstructure at 20°C). The difference between the predicted curves and the experimental ones can have different origins. In the notched specimen the strain rate is not uniform and larger in the notch area, moreover stress triaxiality is higher than in smooth specimen. The, strain rate sensitivity or mechanical anisotropy could explain the observed difference. But, as described in Appendix A, those two phenomena are no observed in our materials. Finally, we chose to keep a simple Voce type law to describe the plastic hardening behavior of the microstructures (see equation 3) but to identify the two fitting parameters Q and b by an inverse method directly on each AE experimental loading curves. Q and b values identified on the AL specimen were used as starting values in the optimization process. The motivation for this lies in the influence of the stress triaxiality ($\tau_\sigma = \sigma_m / \sigma_{MISES}$ with σ_m and σ_{MISES} being the mean and Von Mises equivalent stress respectively) and difference between a uniaxial tensile test and an axisymmetric notch. In the first case, τ_σ equals 1/3 while its magnitude is larger for the notch sample (with a dependence on the notch radius calibrated by Bridgman [28] in the case of a perfect plastic material). As a J_2-flow theory, as adopted here, neglects any volumetric inelastic strain, some of these effects are expected here however and some departure between the un-notched vs notched specimen under tension likely to take place. As our aim is to estimate realistic stress/stain fields in the sample, such effect is accounted for undirectly by fitting the Voce's parameters for the notched specimens for capturing the Force vs relative variation of the notch diameter in a least square sense. The corresponding identification is reported in Table 5.

Microstructure	Temperature (°C)	Notched specimen	R_o (MPa)	Q (MPa)	b (MPa)
Ti	20	Ti-H2-1	300	330	12.7
		Ti-H2-2			
		Ti-H2-3			13.07
	-40	Ti-C2-1	359	330	12.7
		Ti-C2-3			
		Ti-C2-2		350	13.07
Nb	-40	Nb-C2-1	404	380	10.5
		Nb-C2-2			
		Nb-C2-3			
		Nb-C2-4			
NbG	20	NbG-H2-1	346	270	15
		NbG-H2-2			
		NbG-H2-3			
		NbG-H2-4			
	-40	NbG-C2-1	398	237	15
		NbG-C2-3			
		NbG-C2-2		270	16
		NbG-C2-4		290	
CrP	20	CrP-H2-1	324	340	10.6
		CrP-H2-2			
		CrP-H2-3		360	
		CrP-H2-4			
	-40	CrP-C2-1	389	340	10.6
		CrP-C2-2			
		CrP-C2-3		360	
Cr	20	Cr-H2-1	442	330	11
		Cr-H2-2			
	-40	Cr-C2-1	532	319	9.19
		Cr-C2-2			
Cr0	20	Cr0-H2-1	533	282	8.86
		Cr0-H2-2			
		Cr0-H2-3			
		Cr0-H2-4		330	9.94
	-40	Cr0-C2-1	534	310	18
		Cr0-C2-2			
		Cr0-C2-3			
		Cr0-C2-4		330	19

Table 5. Parameters R_o, Q and b identified on the notched tensile tests for each microstructure at 20 °C and -40 °C

Once the constitutive law identified for each microstructure at both temperatures, the stress fields at the onset of failure are extracted, in particular the distribution of the maximum principal stress σ_I along the minimum diameter section. From the identification of the location of the cleavage initiation site on each fracture surfaces, the related critical stress can be determined following the method described in section 2. The obtained average values are reported in table 6.

Microstructure	σ_c at 20 °C (MPa)	σ_c at -40 °C (MPa)
Ti	1110 ± 30	970 ± 40
Nb	x	1490 ± 40
NbG	1160 ± 90	920 ± 90
CrP	1350 ± 140	1170 ± 140
Cr	1330 ± 120	1230 ± 190
Cr0	1110 ± 160	1070 ± 140

Table 6. Critical stress for cleavage fracture for each model microstructure at 20 °C and at – 40 °C.

For all microstructures, the value of σ_c is smaller at -40 °C than those at 20 °C. The critical stresses for the unstabilized microstructures are more scattered than for the stabilized ones. The Cr and CrP microstructures have a similar value for σ_c, slightly larger than the one for Cr0. The Nb microstructure has the largest critical stress at -40 °C and at 20°C no critical stress is measured as the rupture is completely ductile. The Ti-stabilized microstructure has critical stresses similar or smaller to the ones for the unstabilized microstructures. It is difficult to link directly the critical stress measured here to the DBTT obtained from Charpy impact tests. Indeed, for the Nb-stabilized microstructure the two properties seem consistent since the DBTT is the lowest one obtained here and σ_c is the largest one measured among the model microstructures, but for the Ti-stabilized microstructure the values do not exhibit such correlation: its DBTT is smaller than the one of the Cr microstructure but its critical stress is lower too. Actually, the yield strength must be considered too since cleavage rupture is in competition with ductile rupture. In the conditions of our study, ferrite matrix and temperature between -40 °C and 20 °C, plastic deformation always precedes the cleavage rupture [9]. Then, cleavage rupture will take place if the local stress reaches the critical stress, otherwise ductile rupture takes place [8,9,29]. So, the relevant feature is the difference between the critical stress for cleavage and the yield strength that controls cleavage rupture, this is why it seems more appropriate to use the $\sigma_c/R_{p0.2}$ ratio to compare the different microstructures. A good correlation is obtained between this normalized critical stress and DBTT for a given microstructure (see figure 8): DBTT decreases when $\sigma_c/R_{p0.2}$ ratio increases.

In the next section, a more detailed analysis of the data and the fracture surfaces will allow the identification of mechanisms leading to cleavage fracture in each microstructure and then a better understanding of critical stresses measured here.

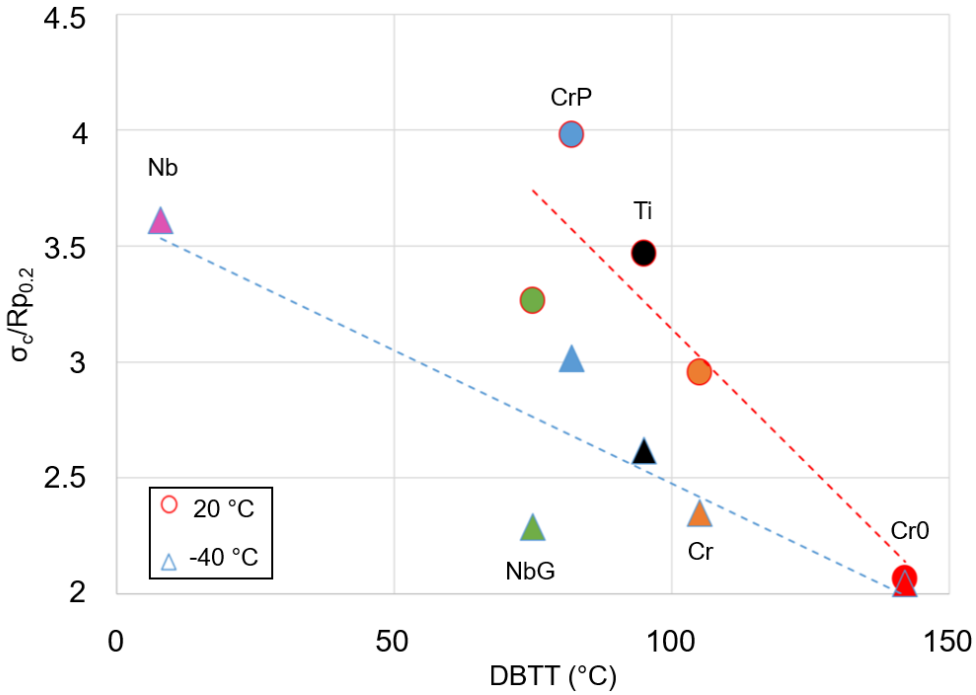

Figure 8. Comparison of normalized critical stress $\sigma_c/R_{p0.2}$ to DBTT.

4. Discussion

In order to better understand the initiation and propagation stages of cleavage for each microstructure, a deeper analysis was conducted based on the observation of fracture surfaces and cross-sections of interrupted AE tensile test samples. For each microstructure, one of the AE tensile test was interrupted just before the failure of the sample and then cross-section observations of the notch area were conducted thanks to sequential polishing every 200 µm along the transverse direction.

a. Stabilized microstructures

Fracture surfaces observations of the stabilized microstructures reveal the presence of a particle at the cleavage initiation site: TiN particle for Ti-stabilized microstructure and Nb(C,N) for Nb-stabilized ones (see figure 9). Previous works on carbon steels proposed a mechanism to interpret the cleavage failure after crack initiation from an intragranular brittle particle [9,16,17]. In this approach, the crack initiated in the particle must cross different microstructure barriers: the particle/matrix interface first, then, after growing inside the hosting grain, the grain boundary in order to propagate into neighboring grains and leading to final failure. Those barriers are associated to critical stresses that are defined within a Griffith's framework for fracture [9,14,16]:

$$\sigma_{p/m} = \left(\frac{4E\gamma_{p/m}}{\pi(1-\nu^2)\phi_p} \right)^{1/2} , \tag{4.1}$$

$$\sigma_{m/m} = \left(\frac{4E\gamma_{m/m}}{\pi(1-\nu^2)\phi_g} \right)^{1/2} , \tag{4.2}$$

where $\sigma_{p/m}$ and $\sigma_{m/m}$ are respectively the critical stresses for particle/matrix interface and grain boundary crossing, and $\gamma_{p/m}$ and $\gamma_{m/m}$ the associated critical surface energies. According to those equations, $\sigma_{p/m}$ depends on the particle size ϕ_p while $\sigma_{m/m}$ depends on the grain size ϕ_g. Then, the limiting stage determines the critical stress for cleavage rupture: σ_c will be either equal to $\sigma_{p/m}$ or to $\sigma_{m/m}$, depending on which one is larger.

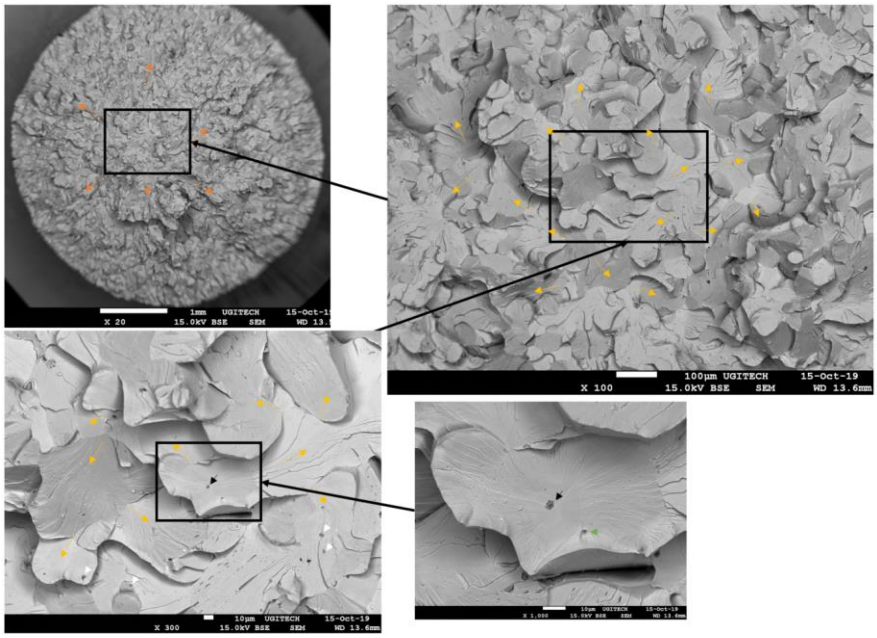

Figure 9. SEM images of the fracture surface of a Ti-stabilized microstructure after AE tensile test at 20 °C. Yellow arrows indicate the cleavage crack propagation directions, black arrow points at a Ti(N,C) particle at the crack initiation site.

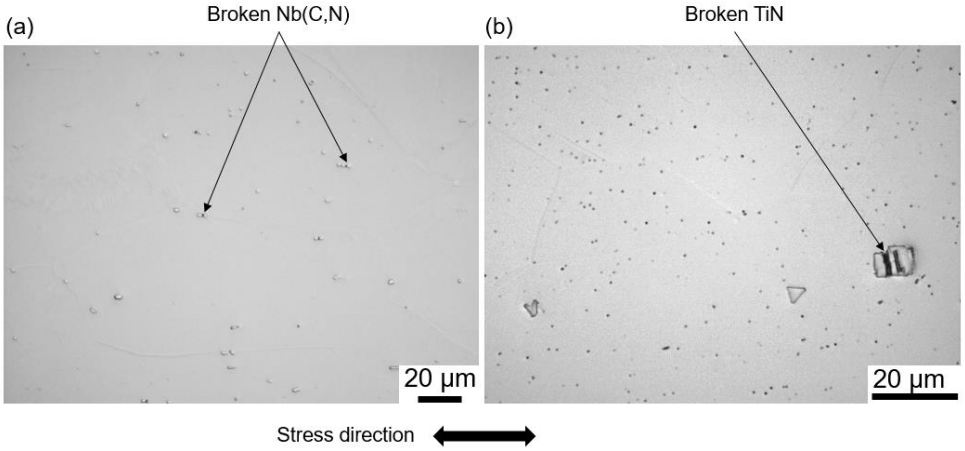

Figure 10. Optical image of cross-section of the notched area after interrupted AE tensile test on (a) Nb-stabilized microstructure at -40 °C and (b) Ti-stabilized microstructure at 20 °C.

The observations of the cross-sections in interrupted AE tensile test samples suggest that, in the stabilized microstructures studied here, the limiting stage is the particle/matrix interface crossing. Indeed, before the final failure, broken particles can be observed, but no arrested crack is visible inside the grains (see figure 10).

According to the multiple barriers model, this means that the critical stress is equal to $\sigma_{p/m}$ and then depends on the particle size (equation 4.1). In figure 11.a the critical stress for cleavage rupture is then plotted against the size of the 2% larger particles in each microstructure: Nb(C,N) in Nb-stabilized microstructures (Nb and NbG) and TiN in Ti-stabilized microstructure. In this graph, the curves corresponding to equation (4.1) are also plotted with different values for the particle/matrix interface energy $\gamma_{p/m}$. This interface energy depends on the interface nature and then the particle chemistry if the matrix is considered the same in each microstructure. At -40 °C, $\gamma_{p/m}$ = 7-8 $J.m^{-2}$ is found to fit the measured critical stresses for the two Nb-stabilized microstructures while a value of 14 $J.m^{-2}$ is obtained for the Ti-stabilized microstructure. At 20 °C, the estimated interface energies are slightly higher: 12 $J.m^{-2}$ for the NbG microstructure and 19 $J.m^{-2}$ for the Ti one. Those interface energies are in agreement with values from previous studies that are in the range of 7 to 30 $J.m^{-2}$ [16,30].

The controlling mechanism for cleavage failure in the stabilized microstructures is identified as the crossing of the particle/matrix interface, and, as a consequence, the particle size is an important parameter. Figure 11.b shows the evolution of the DBTT with the corresponding microstructures. In this figure, we observe that the DBTT increases when the particle size increases, which is correlated to a better resilience of Nb-stabilized microstructures than the Ti-stabilized one. Moreover, it also leads us to conclude that the larger DBTT of the NbG microstructure as compared to the Nb microstructure is due to a larger particle size more than to a larger grain size.

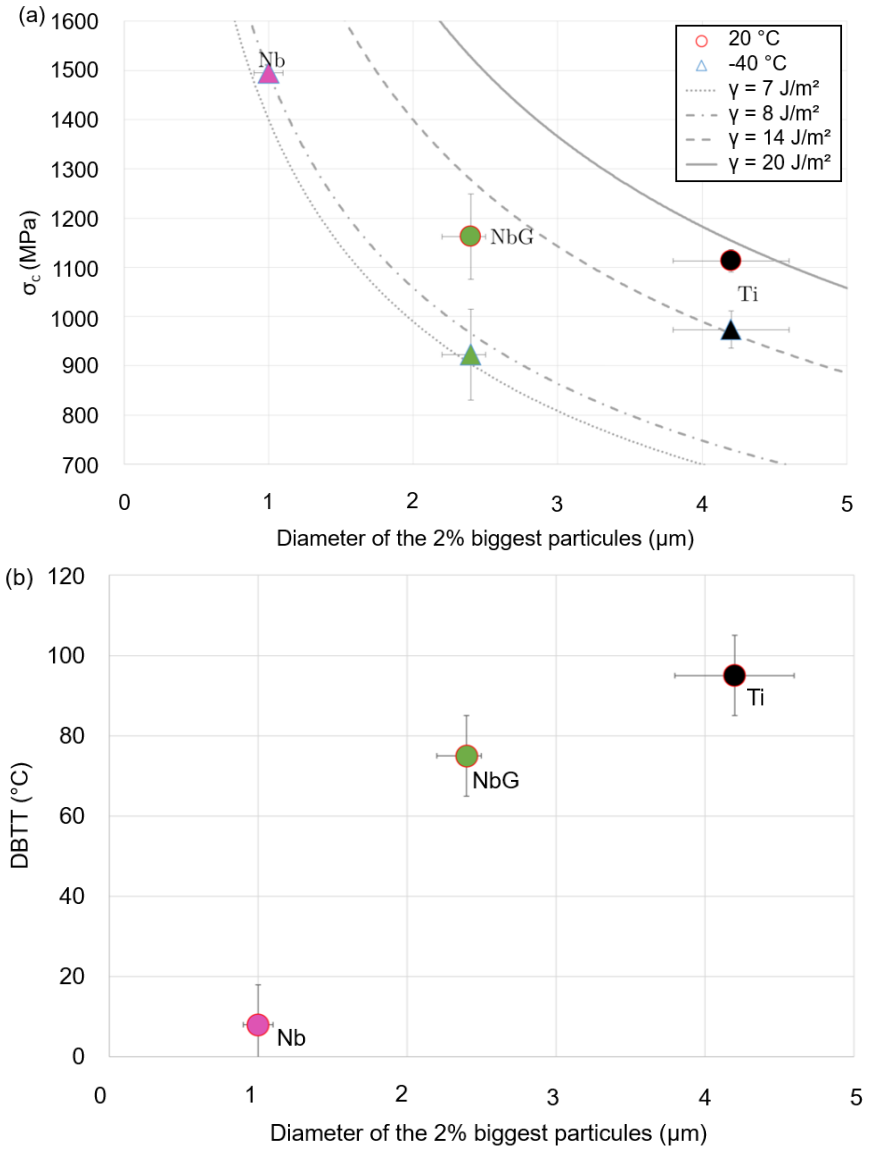

Figure 11. Evolution of (a) the critical stress for cleavage failure and (b) the Ductile to Brittle Transition Temperature with the particle size in the stabilized microstructures.

b. Unstabilized microstructures

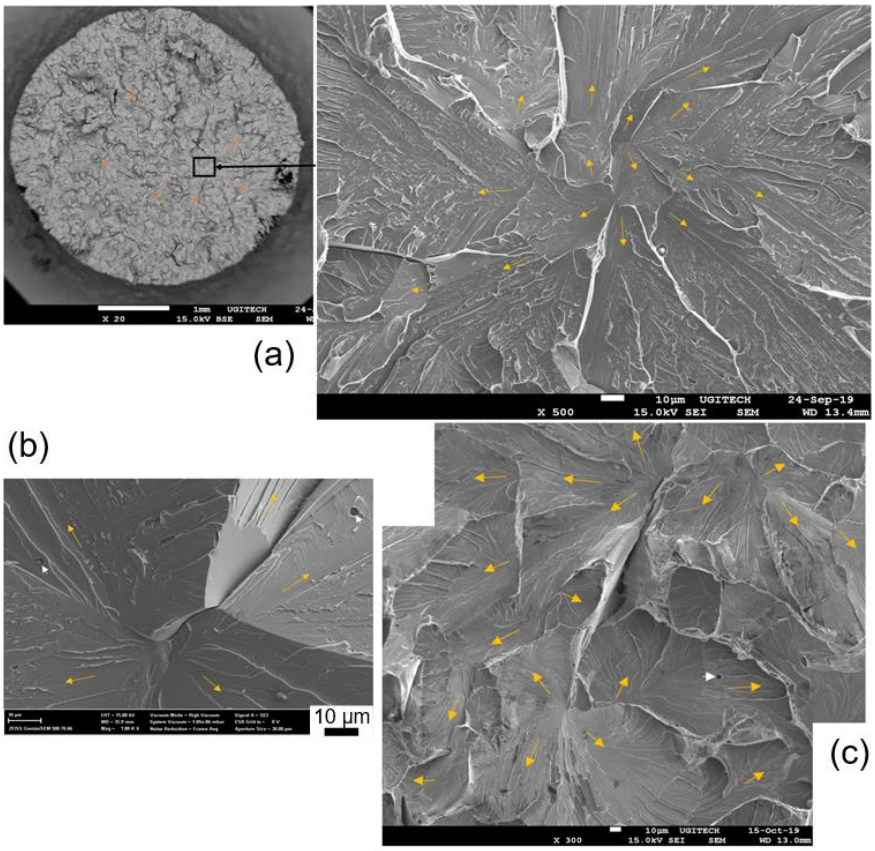

Figure 12. SEM images of fracture surfaces after AE tensile tests on unstabilized microstructures (a) Cr at -40 °C; (b) Cr0 at 20 °C and (c) CrP at 20 °C. Yellow arrows indicate the cleavage crack propagation directions from the initiation sites.

For unstabilized microstructures, a closer look at the initiation sites for cleavage crack reveals the role of the grain boundaries. Indeed, initiation sites correspond to grain boundaries or triple points (figure 12). In some cases, opened cracks out of the plane of the principal crack are also visible (see figure 12.b and 12.c). This indicates that in those structures, the cleavage mechanism is different than the one identified in the stabilized microstructures where cleavage crack initiates at intragranular particles. The Cr0 microstructure do not have intragranular precipitates, while CrP and Cr microstructures have some micrometric intragranular particles [18] but such particles are not detected at the initiation site on the fracture surfaces. Observations of cross-sections from interrupted AE tensile tests on the CrP microstructure show broken particles inside the grains as well as in the grain boundaries (figure 13). Those broken particles do not lead to crack growth inside the matrix, instead to that, they tend to form cavities because of the matrix plastic deformation. More particles are broken along grain boundaries parallel to the tensile direction than in those perpendicular to this direction. Lindeley et al. [31] observed a similar behavior in the case of intergranular cementite particles: elongated carbide particles are more fragmented when the orientation of their long dimension axis gets closer to the tensile loading direction.

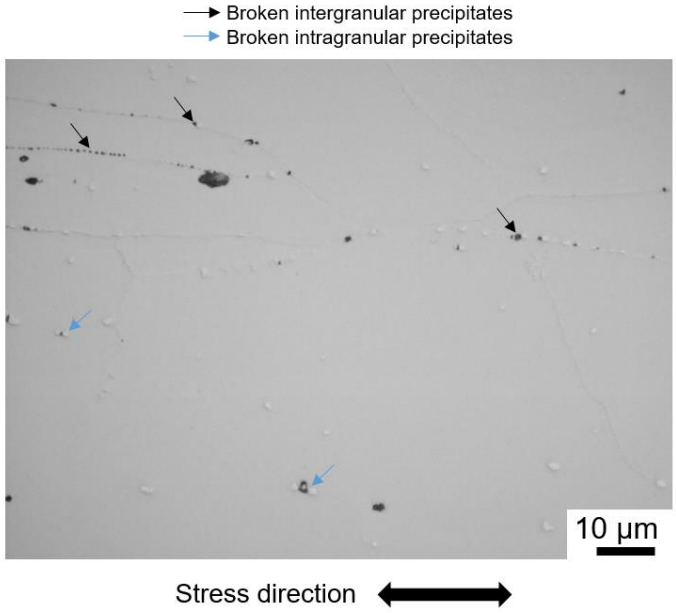

Figure 13. Optical image of a cross-section from an interrupted AE tensile test on the CrP microstructure at 20 °C.

From these observations, the cleavage failure in the unstabilized microstructures seems to be described by the mechanism proposed by Smith [14-15] (see figure 14). In this approach, a carbide particle at a grain boundary is considered: the brittle particle breaks down due to the stress concentration caused by a dislocations pile-up. Then the microcrack propagates into the adjacent grain when sufficient applied stress is attained. By accounting for the two contributions into an energy balance for the micro-crack extension into the matrix, Smith established the following expression:

$$\frac{C_0}{\phi_g}\sigma_c^2 + \tau_e^2\left(1+\frac{4}{\pi}\sqrt{\frac{C_0}{\phi_g}\frac{\tau_i}{\tau_e}}\right)^2 = \frac{4E\gamma_p}{\pi\left(1-\nu^2\right)\phi_g}, \qquad (5)$$

where τ_e is the effective shear stress required for the dislocations pile-up, τ_i the lattice friction shear stress and γ_p the effective surface energy of the matrix, C_0 is the carbide particle thickness. Equation (5) can be rewritten in order to express the critical stress:

$$\sigma_c^2 = \frac{4E\gamma_p}{\pi\left(1-\nu^2\right)C_0} - \tau_e^2\left(1+\frac{4}{\pi}\sqrt{\frac{C_0}{\phi_g}\frac{\tau_i}{\tau_e}}\right)^2. \qquad (6)$$

In equation (6), the first term on the right hand side is similar to a Griffith's approach but here this barrier is diminished by the contribution from the dislocations pile-up at the grain boundary corresponding to the second term.

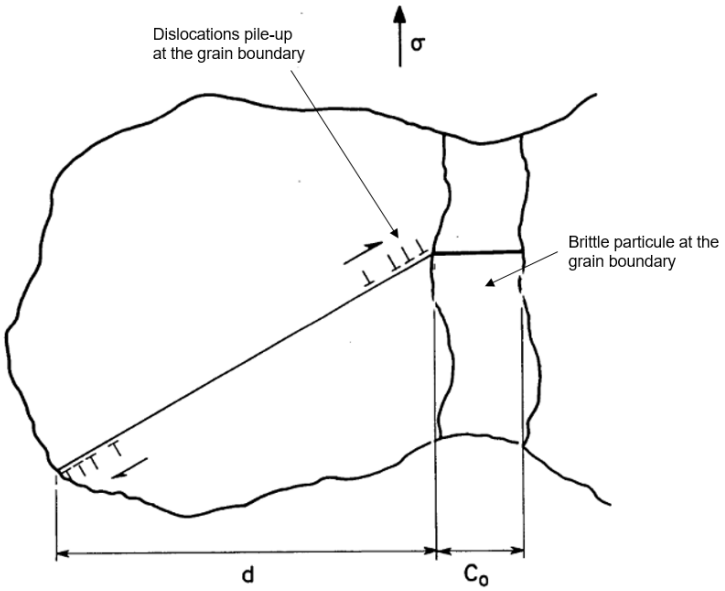

Figure 14. Smith's micro-mechanism for cleavage crack initiation on brittle particle in grain boundary [15].

It is difficult to quantify the critical stress from equation (6) since the values of some of the parameters depend on factors such as temperature, matrix composition or applied stress. The term γ_p corresponds to the surface energy to separate cleavage plan ({100} plans in the ferrite) and the plastic energy dissipated at the crack front [8,32]. The parameter τ_i is the friction shear stress to overcome for a dislocation to move in the matrix. It depends on the temperature and the matrix composition. In particular, when the concentration of carbon and nitrogen in the ferrite solid solution increases the lattice friction shear stress increases [33]. In our microstructures, the 20 % of substitutional solute atoms (Mo and Cr) also increases τ_i. Hence, τ_e depends on the applied stress. Some authors, assuming that cleavage initiates when the applied stress reaches the yielding point, expressed τ_e thanks to the Hall Petch's relation $k_y \phi_g^{1/2}$ where k_y being the Hall Petch coefficient [8,15,33]. Nevertheless, in our microstructures, cleavage failure took place after macroscopic plastic deformation, and this simplification cannot hold. If we cannot quantitatively compare the Smith's model to our results, we can at least qualitatively explain the differences in the magnitude of the critical stress for cleavage in the unstabilized microstructures.

In the Cr and Cr0 microstructures, the thickness of the particles at the grain boundaries is the same, and, if the two alloys have the same composition, the concentration in carbon and nitrogen in the supersaturated matrix is larger in the Cr0 microstructure than in the Cr one [18]. We can then expect a larger lattice friction shear stress τ_i in the Cr0 microstructure than in the Cr one and, according to equation (6), a lower critical stress for cleavage as measured here. The CrP microstructure has been obtained from the Cr microstructure by an extra thermal treatment at 850 °C. While grain size is comparable in both Cr and CrP microstructures, chromium carbides and nitrides precipitation in the CrP microstructure leads to a smaller concentration of carbon and nitrogen in the ferritic matrix and then a smaller τ_i. But at the same time, the particle thickness at the grain boundaries C_0 is larger in the CrP microstructure than in the Cr one. Those two parameters, τ_i and C_0, have opposite effects in equation (6) and they seem to compensate one another in the case of the CrP microstructure, leading to a critical stress for cleavage similar to the one of the Cr microstructure. Finally, the decrease of σ_c when the temperature decreases can also be explained through equation (6) and the dependence of τ_i with temperature: when the temperature

decreases the lattice friction shear stress increases [33] and so the contribution of dislocations pile-up to cleavage failure, leading to higher critical stress for cleavage as observed here.

5. Conclusion

We investigated the initiation of failure by cleavage in ferritic steels and its connection to the microstructure features and in particular the influence of the grain size, the precipitation (type of precipitates and their location inside the grains or at the grain boundaries), the strengthening of the matrix with solute atoms. Careful processing of six microstructures for which one of those parameters was varied resulted in an experience plan. The objective was to establish a correlation between the Ductile-to-Brittle Transition Temperature (DBTT) and the local critical stress for cleavage which is promoted in notched axisymmetric tensile tests.

Depending on the precipitates location, two descriptions are shown able to capture the experimental data: the Smith's model [14,15] in the case of precipitation at grain boundaries or a Griffith inspired approach (for instance [16]) when the precipitates are located inside the grains. For the latter case, the critical stress for cleavage scales with the inverse of the square root of the particle size. In this case, the DBTT increases with the particle dimension. The microstructure barrier to trigger cleavage is found to be the particle-to-matrix stage, or in other words, the onset of crack propagation from the broken particle. The picture is different for the unstabilized microstructures for which particles at the grain boundaries are observed. In this case the Smith's model captures, qualitatively, the variation of the cleavage stress. Here, the "hardness" of the ferritic grains influences the development of the dislocation pile-up that assists the breakdown of the particles at the grain boundaries and subsequent failure.

The study carried out here for ferritic steels shows that a local analysis of failure and detailed analysis of the microstructure is necessary for reliable estimations of the critical stress for cleavage and predictions of the trends in the variation of the DBTT for a given microstructure. It also provides insight on the governing microstructural features that govern the DBTT and is thought to pave the route to the development of alloys with the lowest possible DBTT with appropriate composition and heat treatment.

CRediT authorship contribution statement

L. Jacquet: Methodology, Experiments and Characterizations, Simulation, Writing-original draft. **R. Estevez**: Methodology, Mechanical characterizations, Simulation, Supervision, Writing-review&editing. **M. Braccini**: Mechanical characterizations, Methodology, Writing – original draft. **M. Libert**: Methodology, Characterizations. **N. Meyer**: Methodology, Funding Acquisition. **M. Mantel**: Methodology, Supervision, Writing-review&editing, Project Administration, Funding Acquisition.

Declaration of Competing Interest

The authors declare that they have no known competing financial interests or personal relationships that could have appeared to influence the work reported in this paper.

Acknowledgements

The authors are grateful for the financial support of Ugitech and SIMaP Grenoble INP. Moreover, the authors would like to thanks all researchers and technicians of the SIMaP laboratory and the Ugitech's research center and in particular Aurélien Doitrand for the help on the post-treatment of the correlation images of the AE tensile tests.

Appendix A.

In order to explain the difference between the experimental loading curves on notched samples and predicted one from the plastic law identified on smooth ones two possibilities have been investigated: strain rate sensitivity and mechanical anisotropy. Indeed, in the notched specimen the strain rate is not uniform and larger in the notch area. Then a strain rate sensitivity of our material could explain the observed difference. But strain rate sensitivity tests performed on a similar ferrite microstructure (AISI 444) did not show a noticeable effect in the range of strain rates encountered in this study (see figure A1).

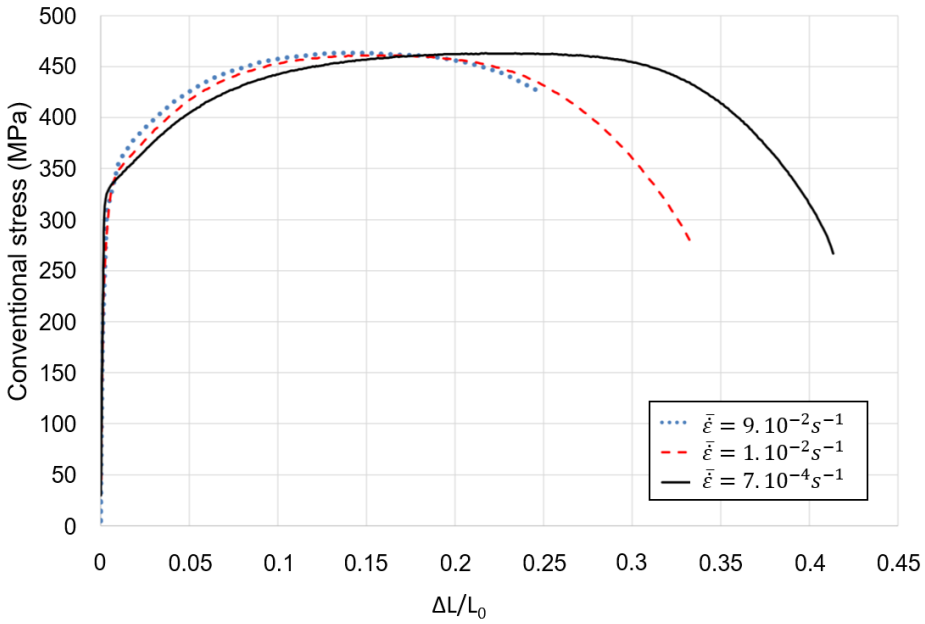

Figure A1. Tensile tests at different strain rate on AISI 444 (18Cr-2Mo-Ti and Nb stabilized)

An anisotropic behavior, due to crystal texture or microstructure anisotropy, could also be invoked to explain the difference of behavior between the predicted curves, based on an isotropic model, and the experimental ones. In the notched specimen the stress triaxiality is higher than in the smooth one and so the contribution from the transverse directions. Observation of the microstructures did not reveal any microstructure anisotropy and X-ray diffraction analysis did not show any preferential crystallographic orientation as it is shown for the Ti microstructure in figure A2.

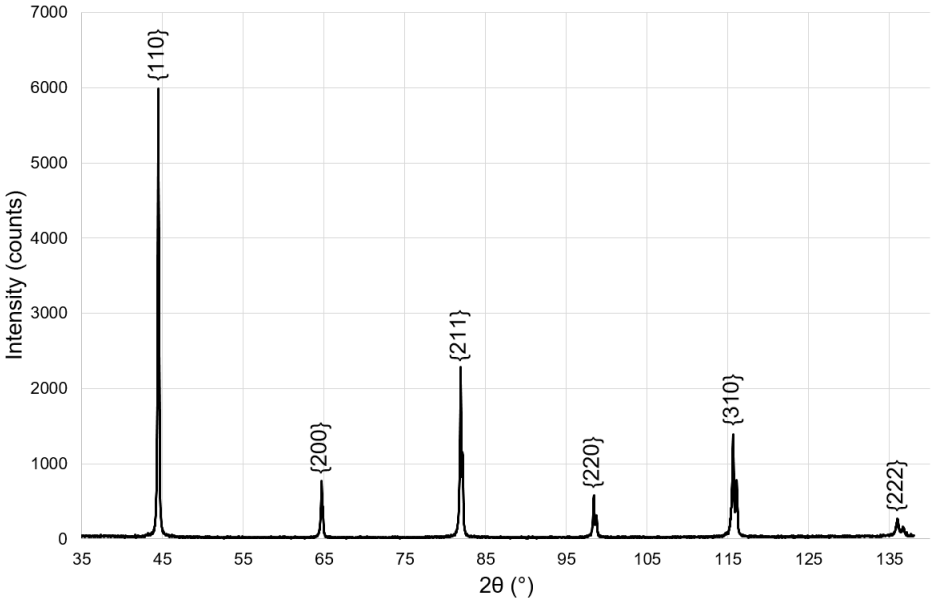

Figure A2. Diffractogram of the X-rays diffraction analysis with a copper anticathode for the Ti microstructure

Data availability

The data can be made available upon request to the corresponding author.

References

[1] Semchyshen, M., Bond, A., and Dundas, H., *Effects of Composition on Ductility and Toughness of Ferritic Stainless*, Climax Molybdenum Development Co, 1972, pp. 239-253

[2] Abo, H., Nakazawa, T., Takemura, S., Onoyama, M., Ogawa, H., and Okada, H., *The role of carbon and nitrogen on the toughness and intergranular corrosion of ferritic stainless steels*, R.Q. Barr (Ed.), Stainless Steel '77, Climax Molybdenum, Golden, CO, 1977, pp. 35-47

[3] Van Zwieten, A. C. T. M. and Bulloch, J. H., *Some considerations on the toughness properties of ferritic stainless steels-A brief review*, International Journal of Pressure Vessels and Piping 56(1) (1993) 1-31

[4] Plumtree, A. and Gullberg, R., *Influence of Interstitial and some Substitutional Alloying Elements*, Toughness of Ferritic Stainless Steels, ASTM STP 706, 1980, pp. 34-35

[5] Sello, M. P. and Stumpf, W. E., *Laves phase embrittlement of the ferritic stainless steel type AISI 441*, Materials Science and Engineering A 527(20) (2010) 5194-5202.

[6] Redmond, J. D., *Toughness of 18Cr-2Mo stainless steel*, ASTM International, 1980, pp.123-144.

[7] Han, J., Li, H., and Xu, H., *Microalloying effects on microstructure and mechanical properties of 18Cr-2Mo ferritic stainless steel heavy plates*, Materials and Design 58 (2014) 518-526.

[8] Miannay, D., *Mécanique de la rupture*, Les éditions de physique, 1995

[9] Pineau, A., Benzerga, A., and Pardoen, T., *Failure of metals I: Brittle and ductile fracture*, Acta Materialia 107 (2016) 426-483.

[10] Zener, C., *Fracturing of metals*, ASM., Cleveland, 1948

[11] Stroh, A., *The formation of cracks as a result of plastic flow*, Proceedings of the Royal Society A 223 (1954) 404-414.

[12] François, D. and Joly, *La rupture des métaux*, Masson et Cie, 1972
[13] Cottrell, A., *Theory of brittle fracture in steel and similar metals*, Transactions of the Metallurgical Society of American Institut of Mining, Metallurgical and Petroleum Engineers 212 (1958) 192-203.
[14] Smith, E., *The nucleation and growth of cleavage microcracks in Mild Steel*, Proc. Conf. Physical Basis of Yield and Fracture, Oxford, Inst. Phys. and Phys. Soc., London, 1966, pp.36-46.
[15] Curry, D. A., *Cleavage micromechanisms of crack extension in steels*. Metal Science 14(8-9) (1980) 319-326.
[16] Linaza, M. A., Rodriguez-Ibabe, J. M., and Urcola, J. J., *Determination of the energetic parameters controlling cleavage fracture initiation in steels*, Fatigue and Fracture of Engineering Materials and Structures 20(5) (1997) 619-632.
[17] Lambert-Perlade, A., Gourgues, A. F., Besson, J., Sturel, T., and Pineau, A., *Mechanisms and Modeling of Cleavage Fracture in Simulated Heat-Affected Zone Microstructures of a High-Strength Low Alloy Steel*, Metallurgical and Materials Transactions A 35(March) (2004) 1039-1053.
[18] L. Jacquet, N. Meyer, M. Libert, F. De Geuser, M. Braccini, R. Estevez, M. Mantel, *Study of cleavage fracture in ferritic stainless steels Part I: Development and characterization of model microstructures*, Materials Science and Engineering A 864 (2023) 144534
[19] Oldfield, W. *Curve fitting impact test data*: *A statistical procedure*. ASTM Stand. News, 3(11), 1975.
[20] Besson, J. and François, D. *Eprouvettes axisymétriques entaillées*, Essais mécaniques et lois de comportement, Hermès Science Publication, Paris, 2001, pp. 319-351.
[21] Henry G. et Roesch L., *Applications pratiques de la microfractographie*, Rev. Met. Paris 66(12) (1969), 841 – 860.
[22] Godin H., Mithieux J.-D., Parrens C., Badinier G., Sennour M., Gourgues-Lorenzon A.-F., *Effects of cooling path and resulting microstructure on the impact toughness of a hot stamping martensitic stainless steel*, Materials Science & Engineering A 742 (2019) 597–607
[23] Abaqus. V6.17 User's Manual. Pawtucket (Rhode Island, USA): ABAQUS Inc.; 2017
[24] Belotteau J., Berdin C., Forest S., Parrot A., Prioul C., *Mechanical behavior and crack tip plasticity of a strain aging sensitive steel*, Materials Science and Engineering A 526(1-2) (2009) 156-165
[25] Marais, A., Mazière, M., Forest, S., Parrot, A., and Le Delliou, P., *Identification of a strain-aging model accounting for Lüders behavior in a C-Mn steel*, Philosophical Magazine 92(28-30) (2012) 3589-3617.
[26] Jaoul, B. *Etude de la plasticité et applications aux métaux*, Dunod edition, 1964.
[27] François, D., *Essais de traction et de compression*, Essais mécaniques et lois de comportements, Hermès Science Publication, Paris, 2001, pp. 89-105.
[28] Bridgman, P.W., *Studies in Large Plastic Flow and Fracture*, Harvard University Press, 1964.
[29] François, D., Pineau, A. and Zaoui, A., *Mechanical behaviour of materials: volume II: fracture mechanics and damage* (Vol. 191). Springer Science & Business Media, 2012.
[30] Kawata, I., Nakai, H., and Aihara, S, *Experimental evaluation of effective surface energy for cleavage microcrack propagation across grain boundary in steels*, Acta Materialia 150 (2018) 40-52.

[31] Lindley, T., Oates, G., and Richards, C. E., *A critical appraisel of carbide cracking mechanisms in ferrite/carbide aggregates,* Acta Metallurgica 18 (1970) 1127-1136.
[32] François, D., Pineau, A. and Zaoui, A., *Mechanical Behaviour of Materials: Volume II: Viscoplasticity, Damage, Fracture and Contact Mechanics* (Vol. 58). Springer Science & Business Media, 1998.
[33] Heslop, J. and Petch, N. J., *The stress to move a free dislocation in alpha iron,* Philosophical Magazine 1(9) (1956) 866-873.